Friction **11**(4): 580–601 (2023)
https://doi.org/10.1007/s40544-022-0622-9
ISSN 2223-7690
CN 10-1237/TH

RESEARCH ARTICLE

Dynamic, thermal, and vibrational analysis of ball bearings with over-skidding behavior

Shuai GAO[1,2], **Qinkai HAN**[2,*], **Paolo PENNACCHI**[1], **Steven CHATTERTON**[1], **Fulei CHU**[2]

[1] *Department of Mechanical Engineering, Politecnico di Milano, Via G. La Masa 1, Milan 20156, Italy*

[2] *State Key Laboratory of Tribology, Department of Mechanical Engineering, Tsinghua University, Beijing 100084, China*

Received: 02 November 2021 / Revised: 05 February 2022 / Accepted: 12 March 2022

Abstract: The term "over-skidding" indicates that the cage rotational speed ratio exceeds the theoretical value as ball purely rolls on the raceway. Different from the skidding phenomenon that occurs in low-load and high-speed bearing, over-skidding usually occurs in large-size angular contact bearings, and it is still difficult to suppress under high load conditions. The main forms of damage to the raceway by over-skidding are spinning and gyro slip. To further explore the vibration characteristics and thermal effects of this phenomenon, a set of over-skidding tests of an angular contact bearing with a bore diameter of 220 mm were conducted on an industrial-size test bench. Through the experiment, the influence of axial load, rotational speed, and lubrication conditions on the occurrence of over-skidding were determined. Based on a previous dynamics model, the heat generation and thermal network models were integrated in the present study to predict the over-skidding and its thermal behavior. The model was validated in terms of the measured degree of over-skidding and temperature rise. The results showed that the degree of over-skidding reaches up to 12% of the theoretical value, and the friction power loss of the ball-pocket accounts for 30% of the total power loss. The analysis of the vibration signal showed a strong correlation between the bearing vibration characteristics and over-skidding behavior, thereby providing a way to indirectly measure the degree of over-skidding.

Keywords: over-skidding; vibration characteristics; dynamic model; power loss; temperature rise

1 Introduction

Rolling element bearings are widely used as core-supporting components in almost all kinds of rotating machinery. Angular contact ball bearings are commonly adopted in applications involving bidirectional axial load, especially for large-sized heavy load equipment such as wind turbines and aero-engines [1, 2]. A representative of bearing operating state, skidding, and over-skidding model can well reflect the dynamics and tribological behavior of the bearing as well as evaluate the smearing damage on the bearing raceways [3, 4]. Thus, an in-depth study on the vibration and thermal characteristics of such large rolling element bearing is highly necessary.

The term "over-skidding" of the bearing was proposed and theoretically explained for the first time by the authors in Refs. [3, 5], which stated that the cage rotational speed is higher than the cage speed under the rolling element's pure rolling state. From the previous studies, the mechanism of over-skidding occurring in large size angular contact ball bearing can be explained as: the frictional driving force in the Hertzian contact area on the raceway needs to provide a gyroscopic moment to maintain the rolling elements rolls purely on the raceway with a nominal contact angle. For large-sized and heavy rolling elements, even if the axial load is large enough, the macro-slip disappears and the gyro-slip still exists. At this time, the self-rotation angle of the

* Corresponding author: Qinkai HAN, E-mail: hanqinkai@hotmail.com

Nomenclature

FPCB	Four point contact ball bearing
CSR	Cage/rotor speed ratio
j	Subscripts for j^{th} rolling element or cage segment
i	Subscripts for inner ring
o	Subscripts for outer ring
A	Characteristic frontal area
a_j, b_j	Hertzian ellipse axis
B_c	Cage width
B_{arc}, B_{Li}	Raceway arc length and inner ring shoulder length
c_{cg}	Cage-guide ring clearance
c_d	Drag coefficient
C_p	Specific heat
D_m	Bearing pitch diameter
D_b	Ball diameter
D_c	Cage diameter
D_{Li}	Inner ring shoulder diameter
D_i, D_o	Raceway diameter of contact point
D_g	Guide ring surface diameter
E	Young's modulus
F_a	Axial load
F_{cg}	Force between cage and guide ring
F_{bp}, f_{bp}	Ball-pocket collision force and friction force
F_{ch}	Oil churning drag force
f_{cg}, M_{cg}	Friction force and moment between cage and guide ring
h_c	Lubricant film thickness
K, h	Heat conductivity and heat transfer coefficient
N_b	Number of rolling elements
N_{Re}, N_{Ta}	Reynolds number and Taylor number
Q	Power loss
u	Relative velocity
V	Volume
x_c, y_c	Cage center coordinate
β_j	Ball orientation angle
ρ_{oil}	Density of the lubrication
ϵ	Cage eccentricity
μ_{cg}	Boundary friction coefficient
μ_v	Viscous friction coefficient
η_0	Lubricant viscosity at a reference temperature
$\eta_j(T, p, \gamma)$	Dynamic viscosity
θ_p	Pocket angular position
ω_g, ω_c	Rotational speed for guide ring and cage
ω_r	Ball self-rotational speed
ω_i	Inner ring rotating speed

rolling element has not yet reached the nominal contact angle. The phenomenon of over-skidding appears macroscopically. Although the phenomenon of over-skidding is rarely involved, the skidding of rolling bearings and its related dynamic behavior [6–13] have been experimentally and theoretically studied. A vibration signal-based method for predicting faulty rolling bearing skidding rate and enhancing fault features has been proposed [7, 8], and the bearing performance degradation is evaluated accordingly. A 3-D nonlinear dynamic model coupled with a thermal expansion analysis to discuss the angular contact ball bearing skidding [4, 5, 10, 14] and cage stability [9, 15] are presented based on the skidding test [16], and the results show that the thrust load and preload can effectively eliminate skidding. In the bearing skidding test, the degree of skidding of the cage revolution can be obtained indirectly as the eddy current sensor [17] or high-speed photographic technology [18] is used to measure the whirling characteristics of the cage in the traditional method. There are also studies on the application of non-contact triboelectric nanogenerators [19] on rolling bearings, which use the changing frequency of the alternating electrical signal generated by the motion of the cage to monitor the cage skidding. Further, the studies on the alternating current generated by the rolling elements in Ref. [20] can be targeted to the skidding ratio analysis of a specific rolling element. Liu [21] and Tu [6] conducted research on the cylindrical roller bearing vibration responses as skidding occurs, and discussed the effects of frictional force [11, 13] and cage pocket type. The results indicate that a proper cage pocket size (tilt angles of 5° and 10° for the front and rear walls can attenuate the skidding degree, and the skidding-induced friction forces are

strongly related to the vibration level. Cao et al. [22] investigated the ball bearing cage stability and cage whirling performance under severe skidding conditions based on the famous dynamic bearing model [23, 24] and cage whirling motion model [25], and found that the whirling stability of the cage decreased significantly when the force of the ball-driven cage was insufficient.

Although the efficiency of rolling bearings is relatively high, for oil-flood-lubricated large-sized ball bearings with the occurrence of skidding and over-skidding, oil churning, friction power loss, and induced temperature rise of the bearing cannot be neglected [5, 26, 27]. The thermal performance and temperature distribution of rolling element bearings under various lubrication conditions were systematically studied. Examples include grease-lubricated ball bearings [28], roller bearings [29], spherical roller bearings [26], oil-air lubricated ball bearings [30], and oil-flood ball bearings [31]. The thermal network method and generalized Ohm's law are widely applied to discontinuous multibody dynamic systems. These studies indicate that a higher grease filling ratio, oil viscosity, as well as higher speed and load lead to a larger temperature gradient, as well as thermally induced stress inside the bearing contact pair [32]. Li et al. [14] found that the friction heat generation from the inner and outer raceways and the bearing total power loss increased as the skidding degree increased, whereas the friction heat generation of the cage-guide ring interactions and ball-oil churning presented a reverse trend. In addition to the frictional effect of the ball-raceways, researchers have found that the degree of ball-cage pocket wear [33] significantly reduces the rotating stability of the cage, and this wear feature has a slight effect on bearing skidding.

To comprehensively explore the over-skidding phenomenon of large-sized rolling element bearing, an advanced rolling bearing dynamic model that integrates the heat generation calculation and thermal network model was established in this study. A ball bearing with a 220 mm bore diameter was tested using a 15 kW test bench. A variety of operating parameters, such as rotational speed, lubrication conditions, temperature, and applied load, which strongly affect the occurrence of over-skidding behavior, were experimentally investigated. The influence of over-skidding on friction power loss was explored using the verified model. Taking cage over-skidding as an entry point:

1) The proposed model for temperature rise and over-skidding prediction was validated by the experimental results. It comprehensively describes the friction loss caused by different bearing components (oil churning or ball-raceway sliding) and the temperature rise caused by the skidding behavior.

2) A strong correspondence between the bearing vibration frequency characteristics and the over-skidding degree was observed. Features such as resonance frequency bands have also been found to distinguish bearing skidding, over-skidding, and pure rolling.

3) This work enriches the skidding studies in terms of vibration correlation, and it verifies the existence of over-skidding behavior by the two aspects of direct measurement of cage rotational speed and vibration characteristic frequency.

2 Dynamic-thermal model

The dynamic-thermal coupled model for predicting bearing over-skidding and thermal behaviors in this study can be divided into three parts:

1) Generalized dynamic modeling of angular contact ball bearing with oil-flood lubrication and ball-cage interactions.

2) Modular solution for the heat generation of bearing skidding, friction, oil churning, etc.

3) Transient temperature of the bearing assembly based on heat generation and thermal network method.

Parts 2 and 3 are wrapped in the dynamic model and simultaneously solved based on the dynamic results of Part 1. The corresponding parts are presented in the following sections.

2.1 Dynamic model

It should be mentioned that the work of this article is aimed at an in-depth and comprehensive experimental study of the over-skidding proposed in Ref. [3]. The dynamic model for predicting the ball bearing over-skidding behavior and ball motion analysis can refer to our group's previous work on the KH-THD and KH-TEHD models [5], including bearing load distribution, raceway driving force calculation, and

elasto-hydro-dynamic lubrication. The relationship between cage over-skidding and ball motion state is presented. In addition, the ball–cage interaction, cage–guide ring hydrodynamic lubrication, and friction effect have been further explored to improve the dynamic model.

A detailed diagram of the cage–guide ring hydrodynamic lubrication and ball–cage interactions is shown in Fig. 1. The coordinate system setting was consistent with that in Ref. [5]. For the oil-flooded cage–guide ring interaction, as the cage collides with the guide ring, that is, the gap reaches the critical oil film thickness h_c of Hertzian contact [34], the contact force, frictional force, and drag moment can be expressed as Eqs. (1)–(3):

$$F_{cg} = \frac{EB_c^{\frac{8}{9}}}{4}\left(\frac{\delta_{cg}}{0.39}\right)^{\frac{10}{9}} \tag{1}$$

$$f_{cg} = \mu_{cg} F_{cg} \tag{2}$$

$$M_{cg} = \frac{1}{2} D_g F_{cg} \tag{3}$$

where $\delta_{cg} = h_c - (\sqrt{x_c^2 + y_c^2} - 0.5c_{cg})$; (x_c, y_c) is the cage center coordinate, c_{cg} is the cage–guide ring clearance, B_c is the cage width, E is Young's modulus, μ_{cg} is the boundary friction coefficient, and D_g is the guide ring surface diameter. As the gap is larger than h_c, the hydrodynamic lubrication between the cage and guide rings can be obtained by the equivalent oil film pressure of the short journal bearing, and the force analysis based on the Reynolds equation can be expressed as Eq. (4):

$$F_{cg.x} = \frac{\pi\eta_0 D_g\left(\omega_g + \omega_c\right)B_c^3\epsilon}{8c_g^2\left(1-\epsilon^2\right)^{\frac{3}{2}}};\ F_{cg.y} = \frac{\eta_0\left|D_g\left(\omega_g + \omega_c\right)\right|B_c^3\epsilon^2}{2c_g^2\left(1-\epsilon^2\right)^2} \tag{4}$$

where η_0 is the dynamic viscosity of the lubricant, ω_g and ω_c are the rotational speeds of the guide ring and cage, respectively, and ϵ is the cage eccentricity. The frictional drag moment of relative sliding is given by

$$M_{cg} = \frac{\pi\eta_0 D_g^3\left(\omega_g - \omega_c\right)B_c}{2c_g\left(1-\epsilon^2\right)^{\frac{1}{2}}} \tag{5}$$

The mechanism of over-skidding was found to be closely related to the orientation angle of the ball self-rotation. The friction force of the ball pocket affected by the ball self-rotation angle was calculated accordingly. The position of the contact point L_{bp} is also considered. The force and moment analysis for the cage in the (x_c, y_c) direction can be described as Eqs. (6)–(8):

$$F_{c.x} = \sum_{j=1}^{N_b}\left(\left(F_{bp.j} + F_{ch.j}\right)\cdot\sin\left(\theta_j + \frac{\theta_p}{2}\right) + f_{bp.j}\cdot\cos\beta_j\cdot\cos\left(\theta_j + \frac{\theta_p}{2}\right) + F_{ch.j}\right) + F_{cg.x} + f_{cg.x} \tag{6}$$

$$F_{c.y} = \sum_{j=1}^{N_b}\left(\left(F_{bp.j} + F_{ch.j}\right)\cdot\cos\left(\theta_j + \frac{\theta_p}{2}\right) + f_{bp.j}\cdot\cos\beta_j\cdot\sin\left(\theta_j + \frac{\theta_p}{2}\right)\right) + F_{cg.y} + f_{cg.y} \tag{7}$$

$$M_c = M_{cg} + \sum_{j=1}^{N_b}\left(F_{bp.j}\left(\frac{D_m}{2} + L_{bp}\right) + F_{ch.j}\frac{D_m}{2}\right) \tag{8}$$

where N_b is the number of balls, $F_{ch.j}$ is the oil churning drag force applied to each pocket, $\theta_p = 2\pi/N_b$, θ_j is the angular position of the pocket, D_m is the pitch diameter, $F_{bp.j}$ and $f_{bp.j}$ are the ball-pocket collision force and friction force, respectively, and β_j is the ball orientation angle.

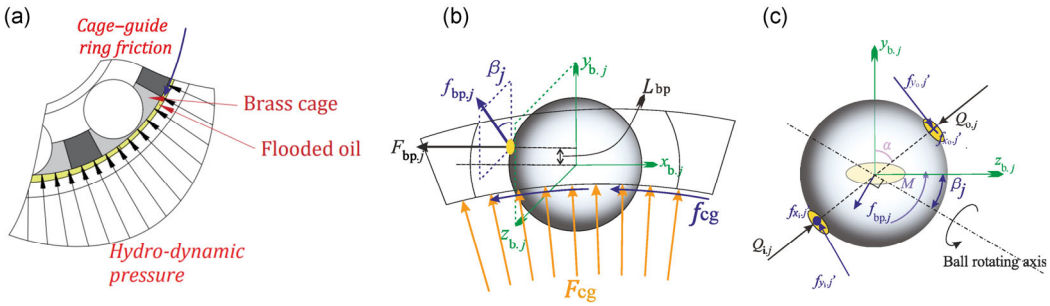

Fig. 1 Schematic diagram for (a) cage–guide ring interaction, (b) ball–cage interaction, and (c) force analysis of ball.

The ball revolution speed can be obtained by Euler's equation as Eq. (9):

$$\frac{\mathrm{d}\omega_{\mathrm{b}}}{\mathrm{d}t}=\frac{1}{J_{\mathrm{b}}+m_{\mathrm{b}}\left(\frac{D_{\mathrm{m}}}{2}\right)^{2}}\left(-\frac{D_{\mathrm{m}}}{2}F_{\mathrm{bp}}-F_{\mathrm{ch.b}}+\frac{D_{\mathrm{i}}}{2}f_{x_{\mathrm{i}}'}+\frac{D_{\mathrm{o}}}{2}f_{x_{\mathrm{o}}'}\right)\leq \tag{9}$$

where m_{b} and J_{b} are the mass and moment of inertia of the ball, $D_{\mathrm{i}}, D_{\mathrm{o}}$ are the raceway diameter of the inner and outer contact points, and $F_{\mathrm{ch.b}}$ is the oil churning drag force applied to the ball, which can be expressed by the experimentally determined drag coefficient c_{d} as Eq. (10):

$$F_{\mathrm{ch}}=\frac{1}{2}c_{\mathrm{d}}\rho_{\mathrm{oil}}u^{2}A \tag{10}$$

where ρ_{oil} is the density of the lubrication media, u is the relative velocity, and A is the characteristic frontal area of the object.

2.2 Heat generation and temperature rise of bearing assembly

The temperature signal was obtained during the test equipment under sufficient lubrication and running at steady state. Figure 2 shows that the eight oil injection nozzles are evenly distributed along the bearing circumferential direction. Meantime, the load applied on the bearing is pure axial and significantly higher than the weight of rotor. Therefore, the temperature gradient in the angular direction was considered to be zero. The heat conduction between the bearing elements and heat convection with oil and atmosphere was calculated in the bearing radial direction. The heat generation of the bearing assembly is mainly a result of friction on the raceway and churning between the rotating parts and viscous oil. The heat generation model included seven modularized heat sources, as shown in Fig. 3.

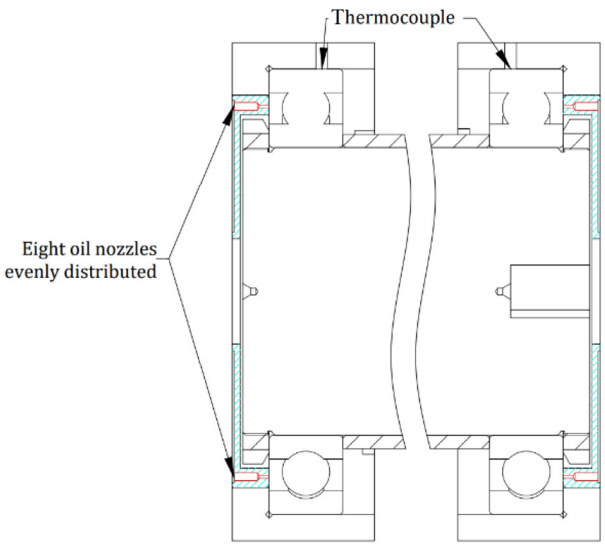

Fig. 2 Schematic diagram for the placement of oil injection nozzles.

2.2.1 *Friction heat from ball-raceway relative sliding*

The friction power loss between the ball and raceways can be calculated by the viscosity of the oil film at the Hertzian contact area and the relative sliding velocity of the ball raceways. The green marks are shown in Fig. 3. The shearing heat of ball which generated in the ball-oil mixing of forward-flow and backward-flow is classified into the ball-oil churning effect presented in Section 2.2.2. The ball-raceway shearing heat can be described as Eq. (11):

$$Q_{\mathrm{br}}=\sum_{\xi}^{\xi=\mathrm{i,o}}\sum_{j=1}^{N_{\mathrm{b}}}\frac{1}{h_{j}}\int_{-a_{j}}^{a_{j}}\int_{-b_{j}\sqrt{1-(y'/a_{j})^{2}}}^{b_{j}\sqrt{1-(y'/a_{j})^{2}}}\eta_{j}\left(T,p,\gamma\right)\cdot\Delta U_{j}^{2}\mathrm{d}y'\mathrm{d}x' \tag{11}$$

where i, o denote the inner and outer raceway contacts, respectively, (a_j, b_j) denotes the Hertzian contact ellipse axis, and $\eta_j(T,p,\gamma)$ is the dynamic viscosity of the oil film, which is determined by the temperature, pressure, and shear rate [35]. ΔU is the relative sliding velocity, which can be referred to in Ref. [36].

2.2.2 *Heat from oil churning*

Owing to the complexity and irregularity of the lubricant flowing inside the narrow space of the bearing, an empirical formula [14, 37, 38] is used to calculate the heat generated by the viscous churning effect (oil churning on balls, cage, and rotating inner ring). Two physical quantities (Reynolds number, N_{Re} and Taylor number, N_{Ta}) describing the fluid flow state, and the viscous friction coefficient μ_{v} can be determined by the Reynolds number and Taylor number of the fluid. Three types of flow patterns are considered:

For laminar flow: $N_{\mathrm{Re}}<2,500$ or $N_{\mathrm{Ta}}<41$:

$$\mu_{\mathrm{v}} = \mu_{\mathrm{l}} = \frac{16}{N_{\mathrm{Re}}} \tag{12}$$

For vortex turbulent: $N_{\mathrm{Ta}} > 41$:

$$\mu_{\mathrm{v}} = 1.3\mu_{\mathrm{l}}\left(\frac{N_{\mathrm{Ta}}}{41}\right)^{0.539474} \tag{13}$$

For Couette turbulent: $N_{\mathrm{Re}} > 2{,}500$:

$$\mu_{\mathrm{v}} = 3.0\mu_{\mathrm{l}}\left(\frac{N_{\mathrm{Re}}}{2500}\right)^{0.85596} \tag{14}$$

where $N_{\mathrm{Re}} = \dfrac{R\omega c}{\eta}$ and $N_{\mathrm{Ta}} = \dfrac{R\omega c}{\eta}\sqrt{\dfrac{c}{R}}$. Considering the cage, ball, and inner ring structure parameters, the oil churning heat generation for the cage, ball, and inner ring can be expressed by

$$Q_{\mathrm{ch.c}} = \frac{\pi\rho_{\mathrm{oil}}\mu_{\mathrm{v}}\omega_{\mathrm{c}}^3 B_{\mathrm{c}} D_{\mathrm{c}}^4}{64} \tag{15}$$

$$Q_{\mathrm{ch.b}} = \frac{c_{\mathrm{d}}\pi\rho_{\mathrm{oil}}\mu_{\mathrm{v}}\omega_{\mathrm{b}}^3 D_{\mathrm{m}}^3 D_{\mathrm{b}} N_{\mathrm{b}}}{256g} \tag{16}$$

$$Q_{\mathrm{ch.s}} = \frac{\pi\rho_{\mathrm{oil}}\mu_{\mathrm{v}}\omega_{\mathrm{i}}^3\left(B_{\mathrm{arc}} + 2B_{\mathrm{Li}}\right)D_{\mathrm{Li}}^4}{64} \tag{17}$$

where D_{c} is the cage diameter, B_{arc} is the raceway arc length, B_{Li} and D_{Li} are the inner ring shoulder length and diameter, respectively, and ω_{i} is the inner ring rotating speed.

2.2.3 *Friction heat from the interaction of cage surface and guide ring*

The friction heat generated from the cage–guide ring interaction can be calculated based on the force analysis described in Section 2.1. The olive marks are shown in Fig. 3.

$$Q_{\mathrm{cg}} = \frac{\mu_{\mathrm{c}}\sqrt{F_{\mathrm{cg}.x}^2 + F_{\mathrm{cg}.y}^2}\,D_{\mathrm{m}}\left(\omega_{\mathrm{g}} - \omega_{\mathrm{c}}\right)}{2} \tag{18}$$

where μ_{c} is the friction coefficient of hydrodynamic lubrication.

2.2.4 *Friction heat from the interaction of ball–cage pocket*

Because the bearing skidding characteristics are emphasized in this study, the collision and friction effects between the cage and the balls cannot be neglected. The total frictional heat generation of the multiple balls can be obtained, as indicated by the blue mark in Fig. 3.

$$Q_{\mathrm{bp}} = \frac{\sum_{j=1}^{N_{\mathrm{b}}}\omega_{\mathrm{r}\cdot j} D_{\mathrm{b}} f_{\mathrm{bp}\cdot j}}{2} \tag{19}$$

where $\omega_{\mathrm{r}\cdot j}$ is the ball self-rotational speed and D_{b} is the ball diameter.

For one bearing assembly, the total friction heat generation can be calculated by the summation of the modularized components above.

$$Q_{\mathrm{tot}} = Q_{\mathrm{br}} + Q_{\mathrm{ch.c}} + Q_{\mathrm{ch.b}} + Q_{\mathrm{ch.s}} + Q_{\mathrm{cg}} + Q_{\mathrm{bp}} \tag{20}$$

2.3 Application of thermal network method

Based on the frictional heat calculation in Section 2.2, the thermal network topology model was applied to the bearing assembly [26, 27, 32]. Some assumptions were proposed in the model. Each temperature node can represent the whole component, and there is no temperature gradient inside. Due to the irregularity

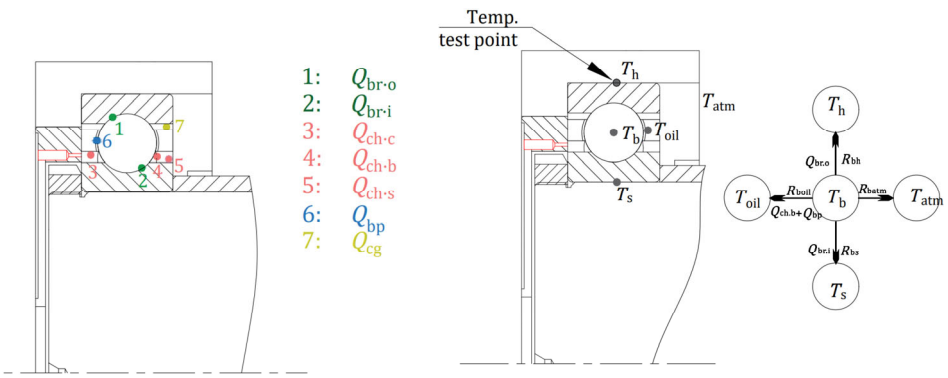

Fig. 3 Heat generation analysis model and thermal network model.

of the cage which is infiltrated by lubricating oil, the oil and the cage are simplified as one temperature node T_{oil} and each node conducts sufficient heat dissipation by the convection of the atmosphere temperature T_{atm}. The thermal node and the example for ball heat conduction are presented in Fig. 3, and the thermal resistance and heat generation rate are shown accordingly. The heat flow for the k^{th} node, which is related to the component temperature variation, can be expressed by

$$Q_k = C_{p.k}\rho_k V_k \frac{dT_k}{dt} \tag{21}$$

where C_p is the specific heat of the element, ρ is the density, and V is the volume of the element. The thermal balance formula can be expressed based on energy conservation as

$$\left[\frac{T_b - T_h}{R_{bh}} + \frac{T_b - T_{oil}}{R_{boil}} + \frac{T_b - T_s}{R_{bs}}\right]\Bigg|_{t=(n+1)\Delta t} = Q_{br} + Q_{bp} + Q_{ch.b} - C_{p.b}\rho_b V_b \frac{T_b\big|_{t=(n+1)\Delta t} - T_b\big|_{t=n\Delta t}}{\Delta t} \tag{22}$$

$$\left[\frac{T_h - T_{atm}}{R_{hatm}} + \frac{T_h - T_{oil}}{R_{hoil}} + \frac{T_h - T_b}{R_{hb}}\right]\Bigg|_{t=(n+1)\Delta t} = Q_{br.o} + Q_{cg} - C_{p.h}\rho_h V_h \frac{T_h\big|_{t=(n+1)\Delta t} - T_h\big|_{t=n\Delta t}}{\Delta t} \tag{23}$$

$$\left[\frac{T_s - T_{atm}}{R_{satm}} + \frac{T_s - T_{oil}}{R_{soil}} + \frac{T_s - T_b}{R_{sb}}\right]\Bigg|_{t=(n+1)\Delta t} = Q_{br.i} + Q_{ch.s} - C_{p.s}\rho_s V_s \frac{T_s\big|_{t=(n+1)\Delta t} - T_s\big|_{t=n\Delta t}}{\Delta t} \tag{24}$$

$$\left[\frac{T_{oil} - T_{atm}}{R_{oilatm}} + \frac{T_{oil} - T_b}{R_{oilb}} + \frac{T_{oil} - T_s}{R_{oils}} + \frac{T_{oil} - T_h}{R_{oilh}}\right]\Bigg|_{t=(n+1)\Delta t} = Q_{ch.c} + Q_{bp} - C_{p.oil}\rho_{oil} V_{oil} \frac{T_{oil}\big|_{t=(n+1)\Delta t} - T_{oil}\big|_{t=n\Delta t}}{\Delta t} \tag{25}$$

The thermal resistance mentioned in Eqs. (22)–(25) is analyzed in detail. It is divided into two categories according to heat conduction and heat transfer. The heat conduction is related to R_{bh} and R_{bs}, which can be simplified as

$$R_{bh} = \frac{2N_b L_{ao}}{K\cdot(\pi L_{ao} L_{bo})}, R_{bs} = \frac{2N_b L_{ai}}{K\cdot(\pi L_{ai} L_{bi})} \tag{26}$$

where L_{ao}, L_{bo} are the axis length of the outer raceway contact area; L_{ao}, L_{bo} are the axis length of the inner raceway contact area; K is the heat conductivity coefficient. For the thermal resistance of heat transfer, it can be expressed as

$$R_{tran} = \frac{L}{h\cdot A} \tag{27}$$

where L and A are the characteristic length and area of the element, respectively, and h is the heat transfer coefficient. The flow state of oil affects the heat transfer coefficient. The empirical value of heat transfer coefficient of lubricating oil ranges from 50 to 1,500 $W/(m^2K)$. Since the eight oil injection nozzles are evenly arranged on the side of the bearing, it is assumed that the lubricating oil is in full contact with the raceway surface and the rolling elements. The characteristic area A for calculating $R_{boil}, R_{hoil}, R_{soil}, R_{hatm}, R_{satm}, R_{oilatm}$ can be described as

$$A_{boil} = N_b\cdot\pi D_b^2; A_{hoil} = \pi D_{Lo} L_h; A_{soil} = \pi D_{Li} L_h \tag{28}$$

$$A_{hatm} = \frac{\pi\left(D_h^2 - D_{Lo}^2\right)}{2} + \pi D_h L_h;$$

$$A_{satm} = \frac{\pi\left(D_s^2 - D_{Li}^2\right)}{2}; A_{oilatm} = A_{boil} + A_{hoil} + A_{soil} \tag{29}$$

where D_h is the outer diameter of bearing house; D_{Lo} is the outer ring shoulder diameter; L_h is the length of bearing house; D_s is the diameter of inner ring.

The transient temperature rise of each node as a function of time can be iteratively solved as the initial temperature distribution is given, and the time step is defined.

3 Test bench and test procedure description

Figure 4 shows an overview of the test bench used to conduct the over-skidding experiments on a four points contact ball bearing. A variable-frequency DC motor with a maximum rotational speed of 1,470 r/min and 15 kW power was used to drive two four-point contact bearings with a bore diameter of 220 mm. The nominal contact angle of the bearing was 40°. The test bearings were mounted on a shaft that was linked to

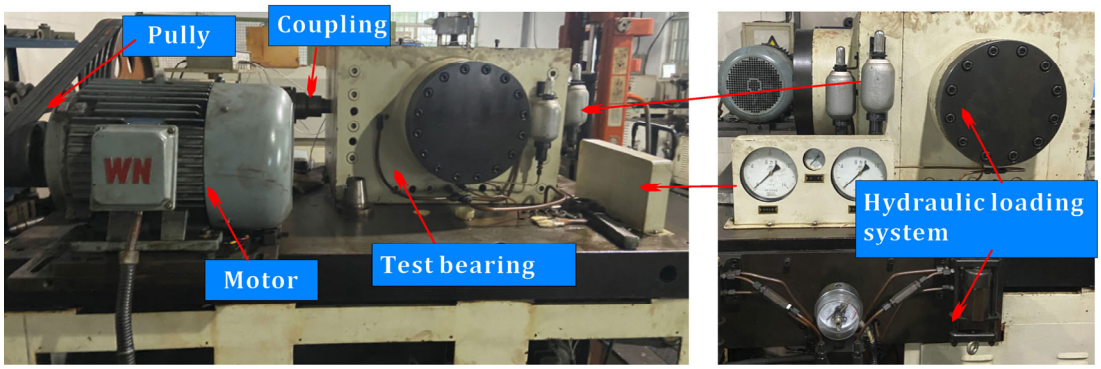

Fig. 4 Overview of the bearing test rig with hydraulic loading system.

the motor shaft by a speed-increasing pulley to create a maximum rotational speed of 1,850 r/min.

The axial force of the bearing was applied by a hydraulic loading system controlled by the counter weight. The range of the axial force was 0–42 kN, and the loading interval was 2 kN. The test rotational speed range was 600–1,800 r/min, and the speed interval was 300 r/min. A group of axial load conditions were tested at each speed condition, and the test bench ran stably for 3 min under each load condition. The experimental procedure is illustrated in Fig. 5. The cage speed and vibration signal were measured in a stable state, and the temperature values were collected every minute. Each group of load tests took 66 min. Considering the weight of the drive shaft, each bearing always bore a radial load of approximately 1 kN.

The sensor placements are shown in Fig. 6. Three magnetic accelerometers were installed in the radial direction of the two bearing housings and in the axial

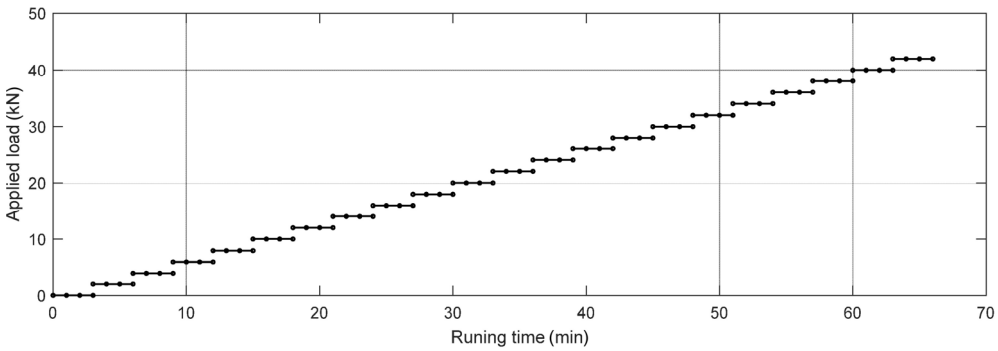

Fig. 5 Experimental procedure of applied load for each speed case.

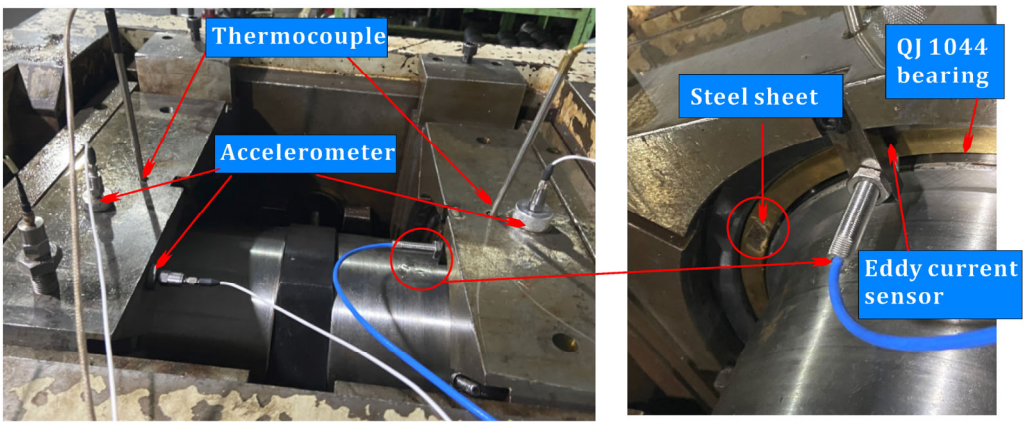

Fig. 6 Placements of three kinds of sensors.

direction of the non-driving end. Two thermocouples were installed on top of the outer ring of the bearing. Figure 7 shows the position of the thermocouple installation. An eddy current sensor was installed perpendicular to the side surface of the cage, and a small steel sheet was pasted on the cage with superglue as a key phase to measure its rotation speed. Vibration signals and cage displacement signals were acquired using the NI CompactDAQ system and NI 9234 modules. The sampling frequency of the vibration signal and displacement signal was 25,600 Hz. The acquisition time was 10s.

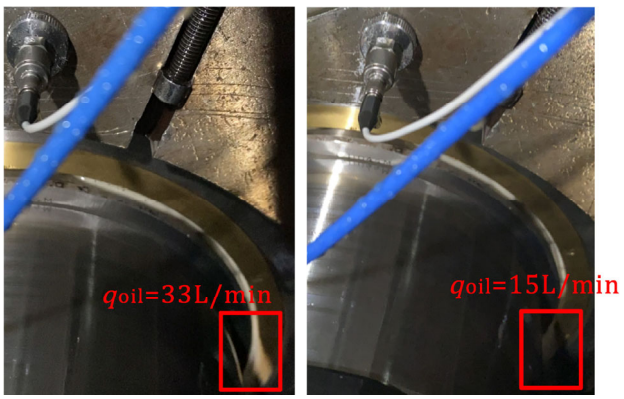

Fig. 7 Oil flood scenes under two oil flow rates (33 and 15 L/min).

To determine the effect of lubrication on over-skidding behavior and the effect of oil flow rate on the power loss of oil churning, an experiment was conducted for two oil supply rates (33 and 15 L/min). The difference in oil overflow is shown intuitively in Fig. 7. Ten sets of experiments with different rotational speeds and oil supply rates were conducted.

4 Discussions on test and model results

4.1 Over-skidding behavior

This section presents the method used for obtaining the cage rotational speed based on the cage axial displacement signal, and a comparison of the cage speed results of the model simulation and the experiment. Figure 8 shows the time-domain signal of the cage axial displacement under three load conditions of ω_i=1,800 r/min. Because a thin steel sheet is pasted on the side surface of the cage perpendicular to the probe, the time interval between adjacent pulses of the displacement signal can be used to determine the rotational speed of the cage.

To set a reasonable pulse threshold line, as shown

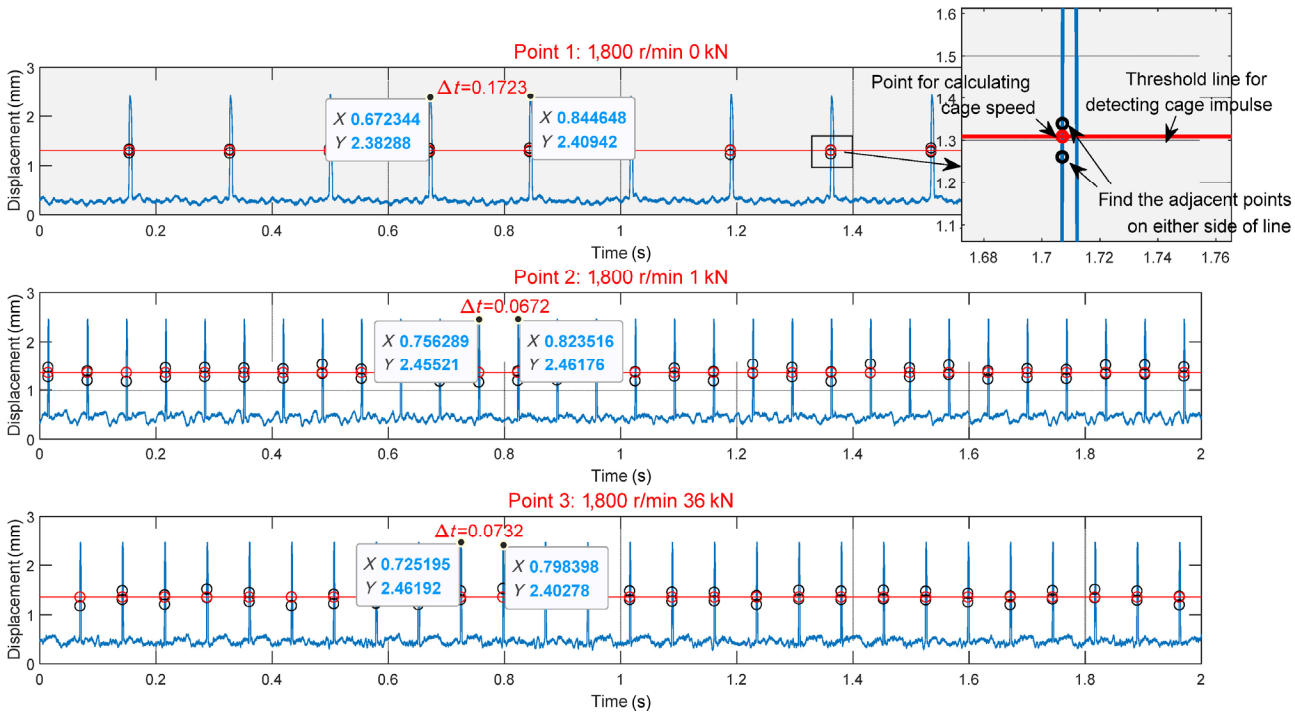

Fig. 8 Time-domain signal of cage displacement and calculation method of cage rotational speed; three axial load condition examples: 0, 1, and 36 kN.

by the red line in Fig. 8, two adjacent data points are located on either side of the threshold line of the rising segment of the pulse (shown as the black dot in the enlarged image of Fig. 8), and linear interpolation was applied to obtain the intersection of the threshold line and the pulse line (red dot). The time interval Δt is obtained from the time difference between two adjacent red dots. The time intervals under these three axial load conditions were $\Delta t = 0.1723$, 0.06672, and 0.0732 s, respectively. The three working conditions correspond to the points marked by the three red circles in Fig. 10(a), and the bearing states are skidding, over-skidding, and approaching the pure rolling state, respectively.

Figure 9 presents the time-varying cage rotor speed ratio (CSR= ω_c / ω_i) under three load conditions based on the above-mentioned method. This indicator reflects the stability of the cage rotation, as well as provides a basis for determining the overall degree of bearing skidding. Combining the standard error value of the 10 s time varying CSR under different working conditions given in Table 1, it can be seen that the cage has the worst stability at $F_a = 0$ kN, and the CSR fluctuation range is approximately 0.006. Meanwhile, the CSR fluctuation was less than 0.001 at $F_a = 36$ kN, and the standard error was only approximately 1/8 of 0 kN. However, even under the worst stability condition, the fluctuation range only accounts for approximately 2.5% of the absolute value. Therefore, the average value of this indicator in the time domain was taken as the measured CSR for the subsequent analysis.

The test results of the CSR as a function of the axial load are presented in Fig. 10. For the test bearing QJ1044, the design limit under oil lubrication was 1,800 r/min. Therefore, the experimental speed was set at 1,800 r/min as the upper limit and 300 r/min as the interval of decrease. The degrees of cage skidding at high, middle, and low speeds were analyzed. The experimental and calculated values for the two oil flow rates were also compared. The black dotted line represents the theoretical speed of the cage (CSR_{th}) as the rolling element's pure rolling. Usually, engineers deem this value as constant [3], but based on the calculation formula of the characteristic frequency of the cage, it is significantly affected by the contact angle of the ball-raceway, especially under varying axial loads. As the theoretical support for the change

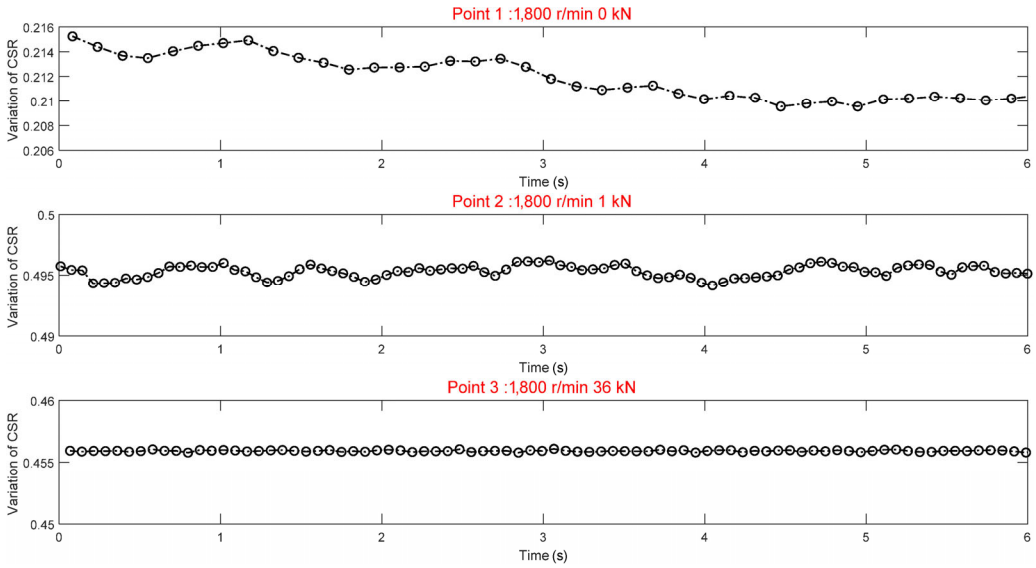

Fig. 9 Time-varying cage-inner ring speed ratio (CSR) calculated by the method in Fig. 8.

Table 1 Examples for the standard error values of the time-varying CSR.

Load conditions (kN)		0	4	8	12	16	20	24	28	32	36	40
Standard error of CSR ($\times 10^{-3}$)	1,800 r/min	0.89	0.29	0.33	0.35	0.39	0.36	0.31	0.20	0.13	0.12	0.09
	900 r/min	0.41	0.23	0.14	0.13	0.16	0.16	0.15	0.14	0.15	0.16	0.15

in CSR_{th}, the upper left of Fig. 10(a) shows the distribution of the ball contact angle when the bearing is subjected to a 1 kN radial load and varying axial loads.

The experimental results show that the bearing exhibits obvious over-skidding behavior, especially at high speeds of 1,800, 1,500, and 1,200 r/min. Compared with the results of Refs. [3, 39], the skidding range of this experiment was relatively small. There was no skidding after F_a >1 kN, and the CSR rapidly grew to an over-skidding state. A possible reason for this is that the bearing always runs under a radial load of approximately 1 kN. The degree of over-skidding reached its peak when F_a was approximately 3 kN, and then slowly weakened with the increase in load until it disappeared. In order to highlight the characteristics of over-skidding, the data of CSR less than 0.4 is shown in the enlarged figure. In terms of both the value and trend, the model results show a favorable agreement with the test results. The maximum degree of over-skidding decreases with the decrease in rotational speed, from 12% CSR_{th} → 10% → 8.5% → less than 1%, as the required axial load for the ball changing from over-skidding to pure rolling is reduced, i.e., the width of the "bulge" is decreased. The effect of the oil flow rate reflected in the model was not as obvious as in the experiment.

The right side of Figs. 10(b) and 10(c) presents the

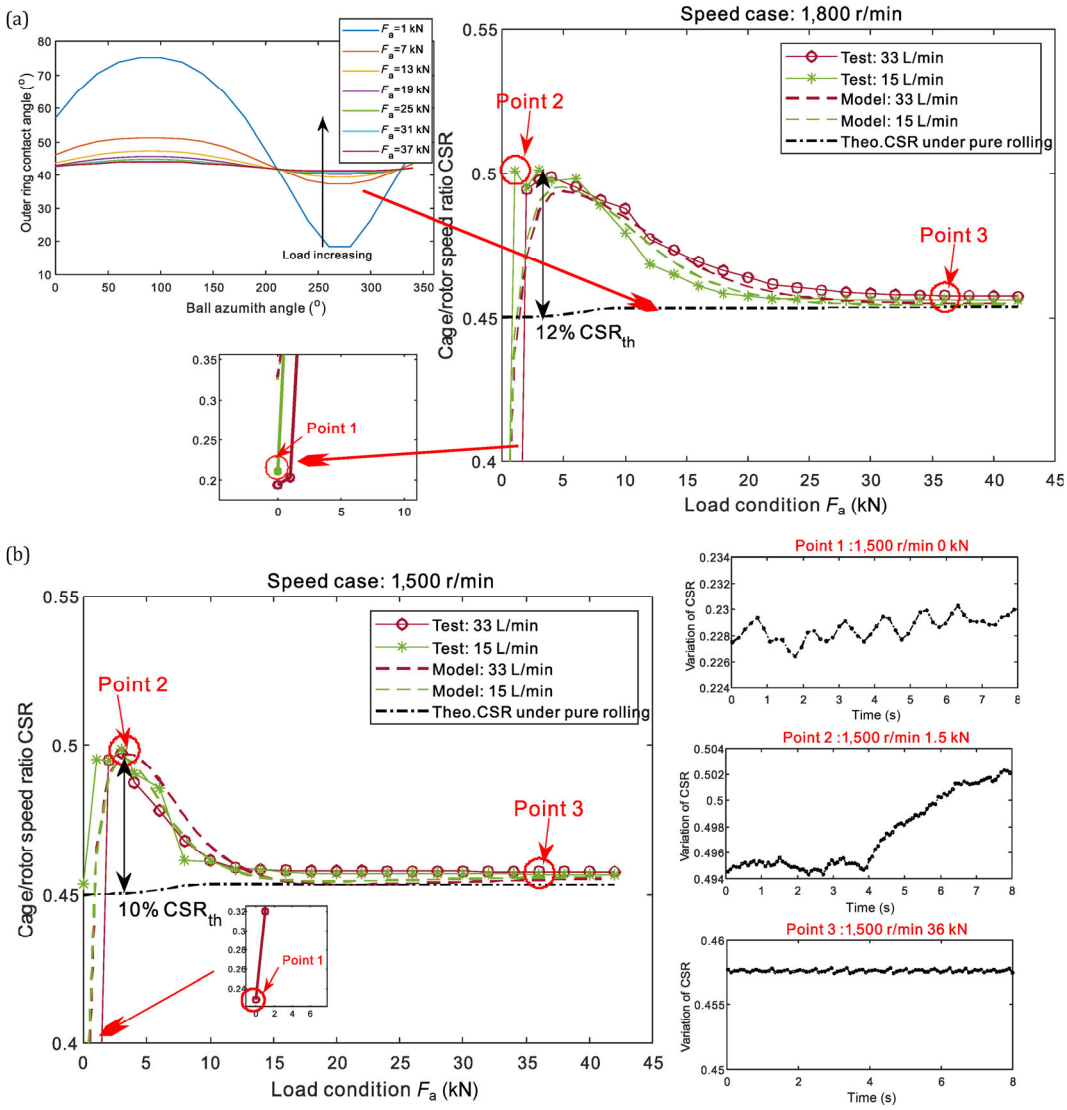

Fig. 10 Comparisons of simulated and tested CSR results as a function of load under five rotational speed cases (600, 900, 1,200, 1,500 and 1,800 r/min) and 2 oil injection flow rates (33 and 15 L/min).

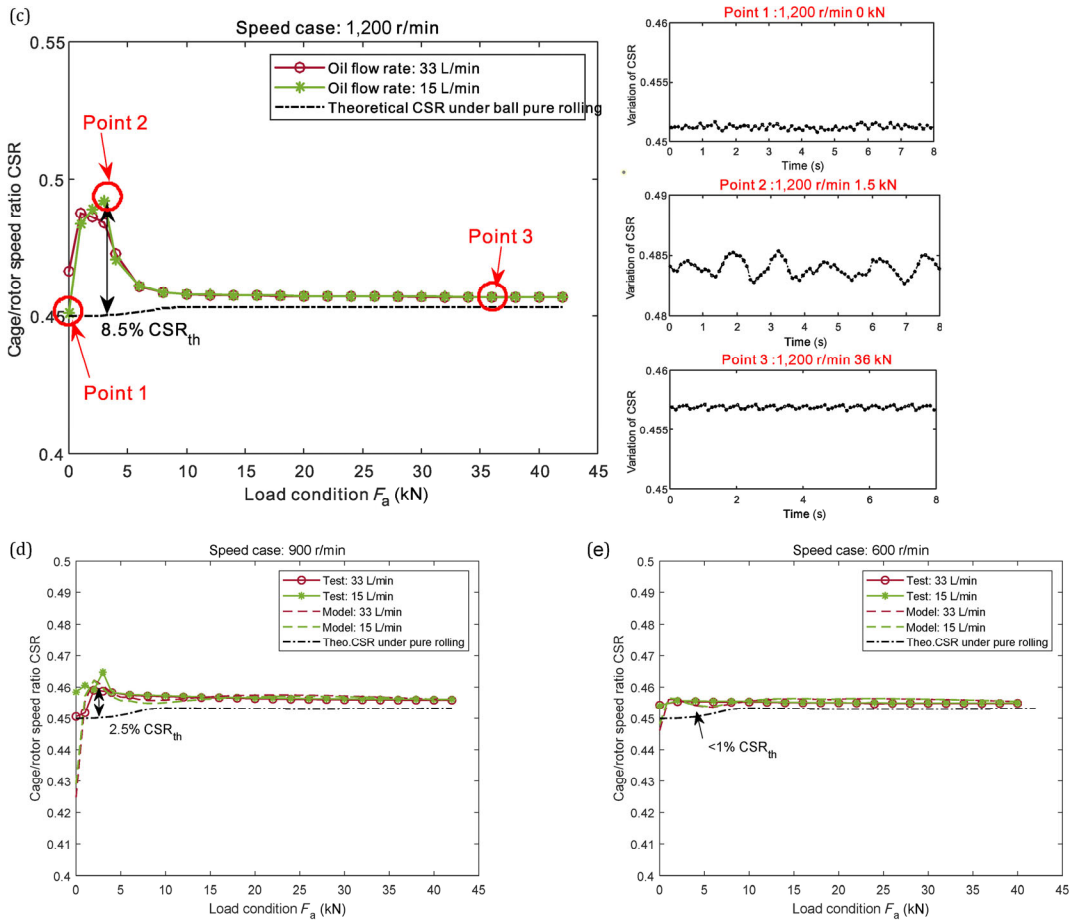

Fig. 10 (Continued)

cage stability characteristics under skidding, over-skidding, and pure rolling. In general, the cage stability of over-skidding was significantly lower than that under pure rolling. Therefore, from the perspective of the stability of the bearing and the possible wear and damage of the raceway, the phenomenon of over-skidding is worthy of attention and should be avoided.

4.2 Vibration characteristics

To explore the characteristics of the skidding and over-skidding behavior in the vibration signal, the acceleration signal collected on the drive-end bearing house is analyzed in this section. Figure 11 presents the time domain, FFT frequency spectra, envelope spectra, and kurtosis diagram of the vibration signal under the test conditions of ω_i =1,800 r/min, F_a =32 kN, and q_{oil} =33 L/min. To better capture the skidding and over-skidding characteristics and ensure the accuracy of the frequency components, the sampling time was set to 10 s, but the time-domain signal only showed the first 1 s for a clear view. Because the featured frequency of the cage is smaller than the rotational frequency of the inner ring, a low-frequency range below 1 kHz is displayed in the frequency spectra.

The maximum kurtosis value of the kurtogram in Fig. 11(d) was 1.62, indicating that the bearing had no obvious impact characteristics. Therefore, the frequency spectra can exclude the fault feature of bearings with raceway or ball defects, as discussed in Refs. [40–42]. The vibration features related to skidding and over-skidding with a lower amplitude are highlighted. The actual rotational speed of the spindle measured by the tachometer in this group of experiments was 1,812 r/min, that is, rotating frequency f_i =30.2 Hz, which corresponds to the characteristic frequency of 30.2734 Hz, as shown in Fig. 11(c). Meanwhile, the frequency component of 13.574 Hz corresponds to $f_i \times \mathrm{CSR}_{th}$ (Fig. 10(a), CSR_{th} =0.452).

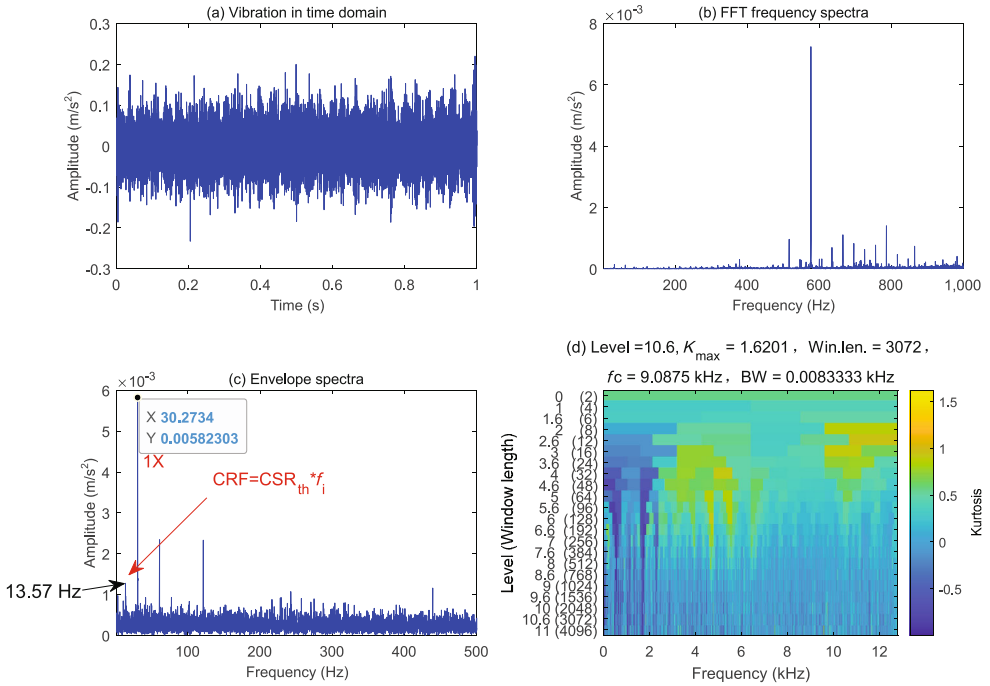

Fig. 11 Signal processing of an example working condition (ω_i =1,800 r/min, F_a =32 kN, and q_{oil} =33 L/min): (a) time domain vibration signal, (b) FFT frequency spectra of the signal, (c) envelope spectra, and (d) Kurtogram.

The three points marked by the red circle in Fig. 10(a) are taken as an example to analyze the vibration characteristics of the bearing under skidding, over-skidding, and pure rolling conditions. Figures 12(a)–12(c) present the FFT spectra and envelope spectra under these three axial load conditions (F_a = 0, 1, and 36 kN). Similarly, the actual spindle rotating frequency f_i =30.2 Hz.

First, for Point 1 showing obvious skidding, the CSR=0.22 is shown in Fig. 10(a); thus, the cage rotation frequency is CSR × f_i =6.732 Hz. Correspondingly, the characteristic frequency of 6.93 Hz appears in Fig. 12(a), which is very close to the cage rotational frequency measured by the eddy current sensor. Compared with the theoretical rotation frequency CRF_{th} =13.6 Hz, the degree of skidding can be evaluated. The sidebands of the spindle frequency with the cage rotation frequency as the interval (such as $2xf_i - 1$xCRF) appear in the envelope spectra. For Point 2 showing over-skidding, the measured CSR=0.501 is shown in Fig. 10(a), the CRF is 15.13 Hz, which is close to the 14.94 Hz appearing in Fig. 12(b). The CRF was significantly larger than CRF_{th} . The harmonic components of (1xCRF, 2xCRF, 3xCRF, etc.) and the sidebands of $2xf_i + 1$xCRF are shown in the envelope spectra, indicating that the over-skidding behavior of the cage can be well reflected by the vibration signal, and the existence of the over-skidding phenomenon is verified from the perspective of indirect measurement. This finding also provides ideas for equipment that cannot directly measure the rotational speed of a cage due to being limited by space.

Comparing the envelope spectra of Point 3, it is found that the characteristic cage frequency of 13.67 Hz is close to CRF_{th} , which can be considered to be the pure rolling state. This is consistent with the measured data shown in Fig. 10(a). The features of the frequency spectra were also informative. As skidding and over-skidding occur at Points 1 and 2, respectively, the spectral components are complex and messy, as shown by the red ellipse in Figs. 12(a) and 12(b). This corresponds to the cage speed stability level shown in Fig. 9. 0 kN had the worst stability, and the frequency band was the messiest. In comparison, the frequency spectra of Point 3 in the pure rolling state were simpler, and the cage had the best stability.

For the rotational speed conditions where the degree of over-skidding is less significant, such as 900 r/min, the same spectrum analysis is shown in Fig. 13. It can be seen that the featured frequency of the cage in

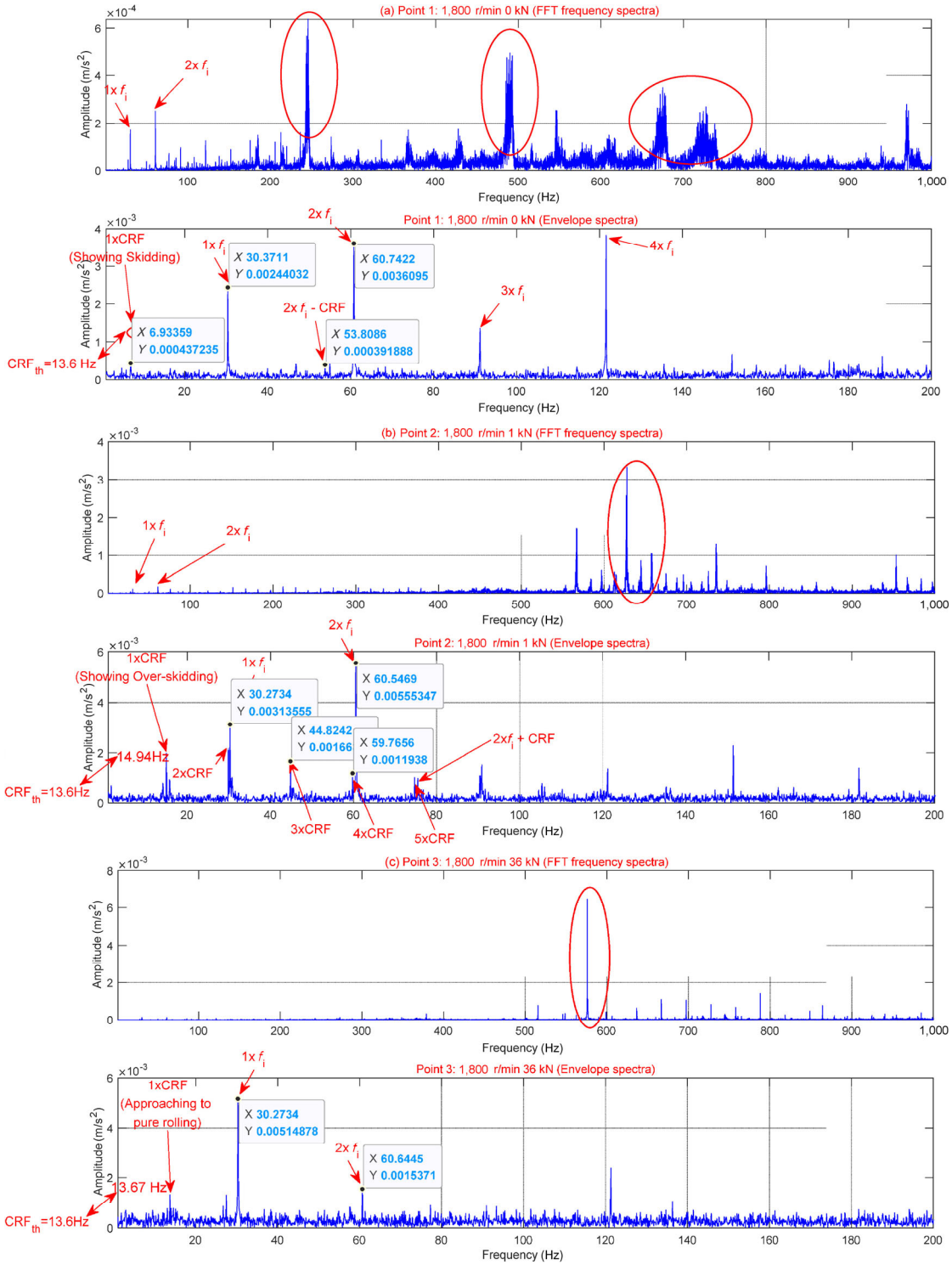

Fig. 12 FFT frequency spectra and envelope spectra of vibration signal of three axial load condition. (a) F_a=0 kN, (b) F_a=1 kN, and (c) F_a=36 kN.

Point 2 is 6.93 Hz, which is slightly higher than CRF_{th} = 6.83 Hz, indicating a low degree of over-skidding. Similarly, in the FFT spectra, there are clustered frequency bands in the test at Point 2, where over-skidding occurs.

In addition to the frequency spectra characteristics of over-skidding and skidding, the overall vibration intensity level of each test condition was evaluated.

Based on the root mean square of the vibration acceleration, the vibration level indicator can be expressed as $a_c = 20\lg a_{rms} / a_0$, where a_0 is the reference acceleration. Figure 14 presents the bearing vibration level for each operating condition under the two oil injection flow rates. The results show that an increase in speed has a significant effect on the increase in the vibration level. In general, the increase in axial load causes the overall vibration level to increase slightly, but in ranges where there is over-skidding, the vibration tends to weaken as the over-skidding is attenuated, as shown in the figure at the working condition of ω_i=1,800 r/min and F_a = 0–10 kN. Comparing the two oil flow rates, the vibration level at low flow rates was lower. The weakening of the injection shock to the ball and cage is an important factor.

4.3 Thermal behavior

In industrial-grade large-sized bearings, rising temperature and power loss of the bearing due to oil churning and skidding behavior are considerable. The thermal behaviors of the bearing are discussed in this section based on the heat generation model

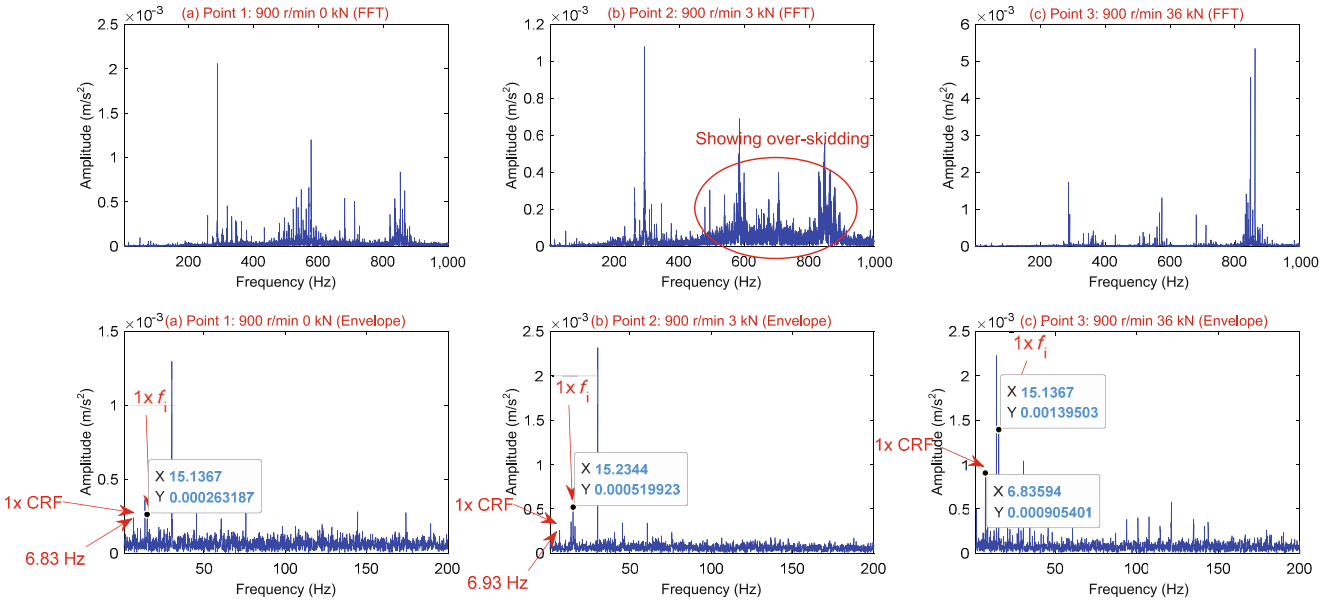

Fig. 13 FFT frequency spectra and envelope spectra of vibration signal of 900 r/min.

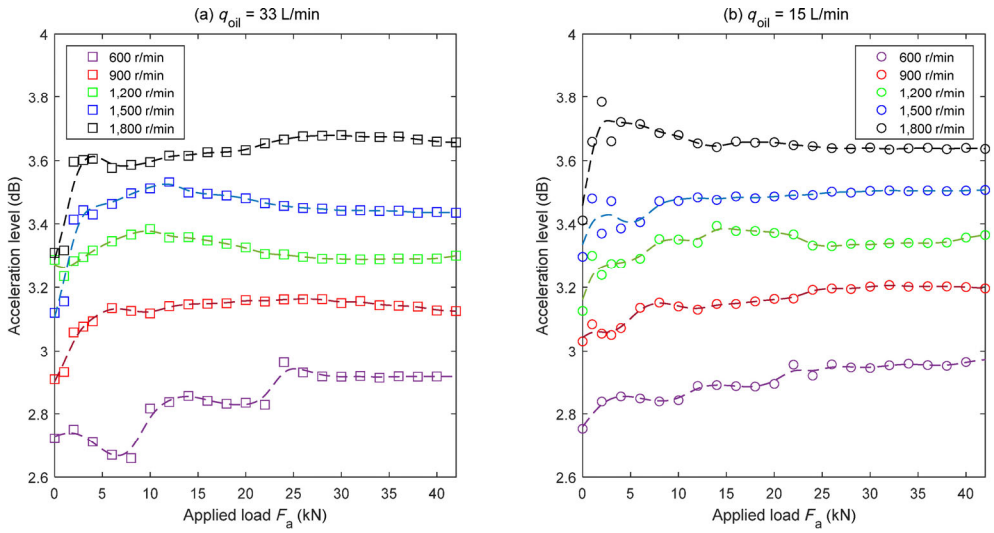

Fig. 14 Acceleration level of each test condition: (a) oil flow rate q_{oil} =33 L/min, and (b) q_{oil} =15 L/min.

and the bearing temperature rise measured in the experiment.

Taking the test group of ω_i=1,800 r/min and q_{oil} = 33 L/min as an example, Fig. 15 shows the power loss of each component (oil churning, relative sliding, etc.) calculated by the model. The stacked histograms represent the total power losses. For the sake of comparison, the heat generation on the vertical ordinate is normalized to a percentage based on the largest value, which is the 3 kN working condition in this calculation. The power loss of each heat generation module is expressed in different colors, and the value in percentage is presented in the attached table of the figure. From the perspective of the total power loss level, it is consistent with the trend of the value of CSR as the axial load increases. The friction loss of the ball–pocket is close to 30%, which is significant in the working conditions of over-skidding. Among these six heat generation modules, the power loss of oil churning is relatively high, accounting for approximately 60%–80%; however, the total amount of oil churning loss does not change significantly with the disappearance of over-skidding. The power loss caused by the ball–raceway's relative sliding and spinning gradually decreases with the increase in axial load.

The calculated CSR value is presented in Fig. 15 as a reference. At the axial load condition of the point marked by the red circle, from a macro point of view, the cage speed is equal to the theoretical value of the cage speed, which means that there is no skidding or over-skidding. However, both the total power loss and skidding heat generation are extremely high under this working condition. The no-skidding state is a false appearance. This kind of ideal state that appears to be pure rolling in a macroscopic view is extremely destructive to the bearing. This is one of the important reasons why the over-skidding phenomenon should be noticed and investigated.

Figures 16(a) and 16(b) compare the total power loss of a single bearing under the two oil injection flow rates. The values calculated by the heat generation model under all test conditions are presented as two histograms. The maximum power loss value was chosen as the reference. The result shows that the total power loss of ω_i=600 r/min is approximately 1/5 of ω_i=1,800 r/min. As shown in Fig. 10, the degree of over-skidding at low speed is relatively low, and this feature is also reflected in the power loss. As the axial load varies, the fluctuation range of the total power loss at a low rotational speed is far less significant than that at a high rotational speed. The power loss

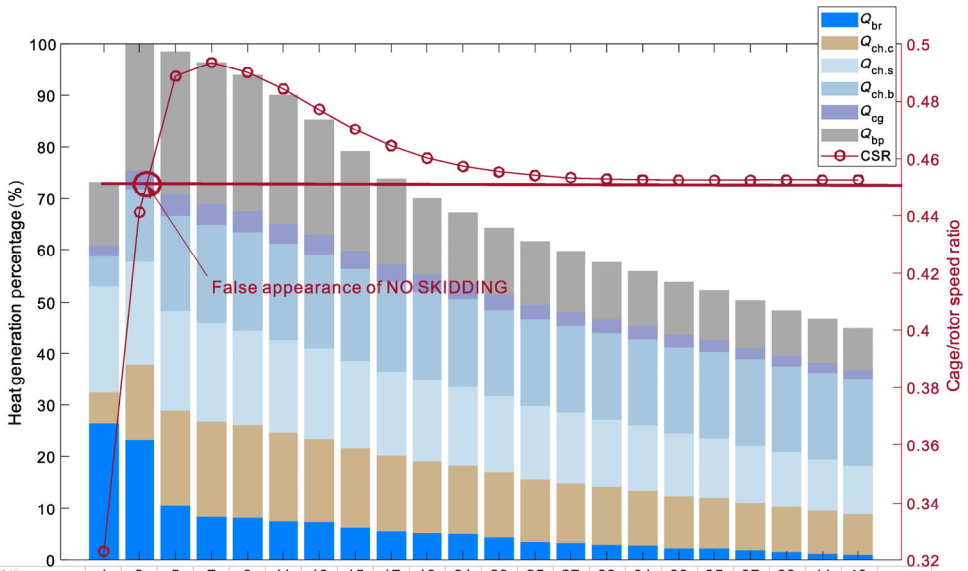

Load (kN)	1	3	5	7	9	11	13	15	17	19	21	23	25	27	29	31	33	35	37	39	41	43	
Ball–Raceway	26.5	23.3	10.7	8.4	8.2	7.6	7.3	6.3	5.6	5.2	5.1	4.3	3.6	3.3	3.0	2.9	2.3	2.3	1.9	1.6	1.2	1.0	
Cage churning	5.9	14.4	18.2	18.4	17.8	17.1	16.2	15.3	14.5	13.8	13.2	12.6	12.1	11.6	11.1	10.6	10.2	9.7	9.3	8.8	8.4	7.9	
Inner ring churning	20.6	20.1	19.5	19.0	18.5	17.9	17.4	16.9	16.3	15.8	15.3	14.7	14.2	13.7	13.1	12.6	12.0	11.5	11.0	10.4	9.9	9.4	Power
Ball churning	5.8	14.2	18.3	19.1	19.0	18.7	18.3	17.9	17.5	17.2	17.0	16.9	16.8	16.8	16.7	16.7	16.7	16.7	16.7	16.7	16.7	16.7	loss (%)
Cage–Guide ring	2.0	3.6	4.2	4.2	4.0	3.9	3.7	3.6	3.4	3.2	3.1	3.0	2.9	2.8	2.7	2.5	2.4	2.3	2.2	2.1	2.0	1.9	
Ball–Pocket	12.2	24.3	27.5	27.3	26.4	24.8	22.2	19.2	16.6	14.8	13.6	12.8	12.1	11.6	11.1	10.6	10.1	9.7	9.3	8.8	8.4	7.9	

Fig. 15 Example for the total and modular power loss of the bearing, with the CSR result as a reference.

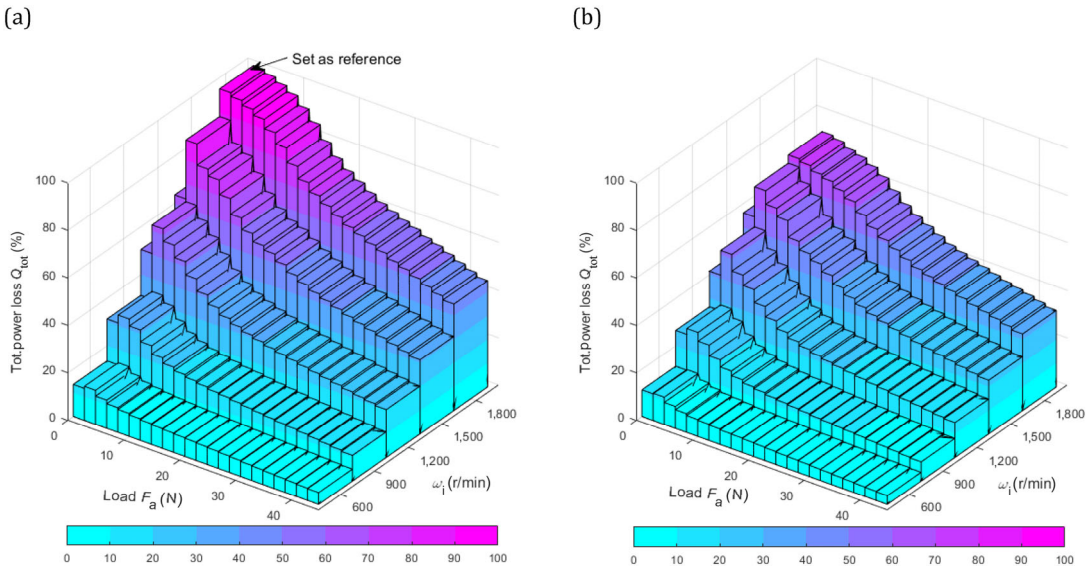

Fig. 16 Normalized total power loss for test conditions: (a) oil flow rate q_{oil} =33 L/min, and (b) q_{oil} =15 L/min.

always reaches the maximum when the axial load conditions are between the skidding and over-skidding peaks, and then it gradually decreases. The total power loss under the oil flow rate of q_{oil} =15 L/min was approximately 75% of q_{oil} =33 L/min. This is mainly because the power loss of oil churning is considerably reduced after the oil quantity is reduced, considering that the cage-oil churning, balls-oil churning, and inner ring-oil churning account for 60%–80% of the total power loss.

The contour diagrams of the power loss of the six components in the heat generation model as a function of the rotational speed and axial load are shown in Fig. 17. The two contour diagrams in each red box are a comparison of the two oil injection flow rates. The maximum value of the color bar is 25% of the maximum power loss (reference point in Fig. 16). Analyzing one by one, the ball-pocket interaction Q_{bp} and the friction power loss of the cage-guide ring Q_{cg} have the same trend as the change in working conditions. However, the power loss of the cage-guide ring interaction Q_{cg} is the lowest among the six components, accounting for only approximately 1/5 of Q_{bp}. Because Q_{bp} and Q_{cg} are strongly related to the ball self-rotational speed and the cage rotational speed, they reach the peak values at the occurrence of the most severe over-skidding degree.

The heat generation of the ball–raceway interaction Q_{br} is strongly related to the relative sliding speed between the ball and the raceway. Q_{br} reaches its peak when the axial load is set to zero, and severe skidding occurs. Because the formation mechanism of over-skidding comes from the fact that the spinning speed and orientation angle of the ball self-rotation do not reach the ideal state, the effect of over-skidding on Q_{br} is not significant compared to the skidding caused by linear sliding.

The oil churning power loss on the cage, balls, and inner ring can be classified into one category. The oil churning loss of the inner ring $Q_{ch.s}$ mainly depends on the speed of the inner ring. The temperature rise and oil viscosity thinning caused by the increase in the axial load slightly reduce the $Q_{ch.s}$, which is in agreement with intuitive expectations. The oil churning power loss of the ball $Q_{ch.b}$ and cage $Q_{ch.c}$ mainly depends on the revolution speed of the ball and the cage, as well as the viscosity characteristics of the lubricant; thus, their contours are similar to the variation trend of Q_{bp}, both reaching the maximum value under the most severe over-skidding states. Under an oil flow rate of q_{oil} =15 L/min, each power loss component is reduced to a certain degree.

Figure 18 presents the temperature rise comparison between the experimental results and the calculated results based on the heat generation and thermal network models. The tested point is located at the outer ring surface of the bearing, which corresponds to T_h in the thermal model. The results of the two

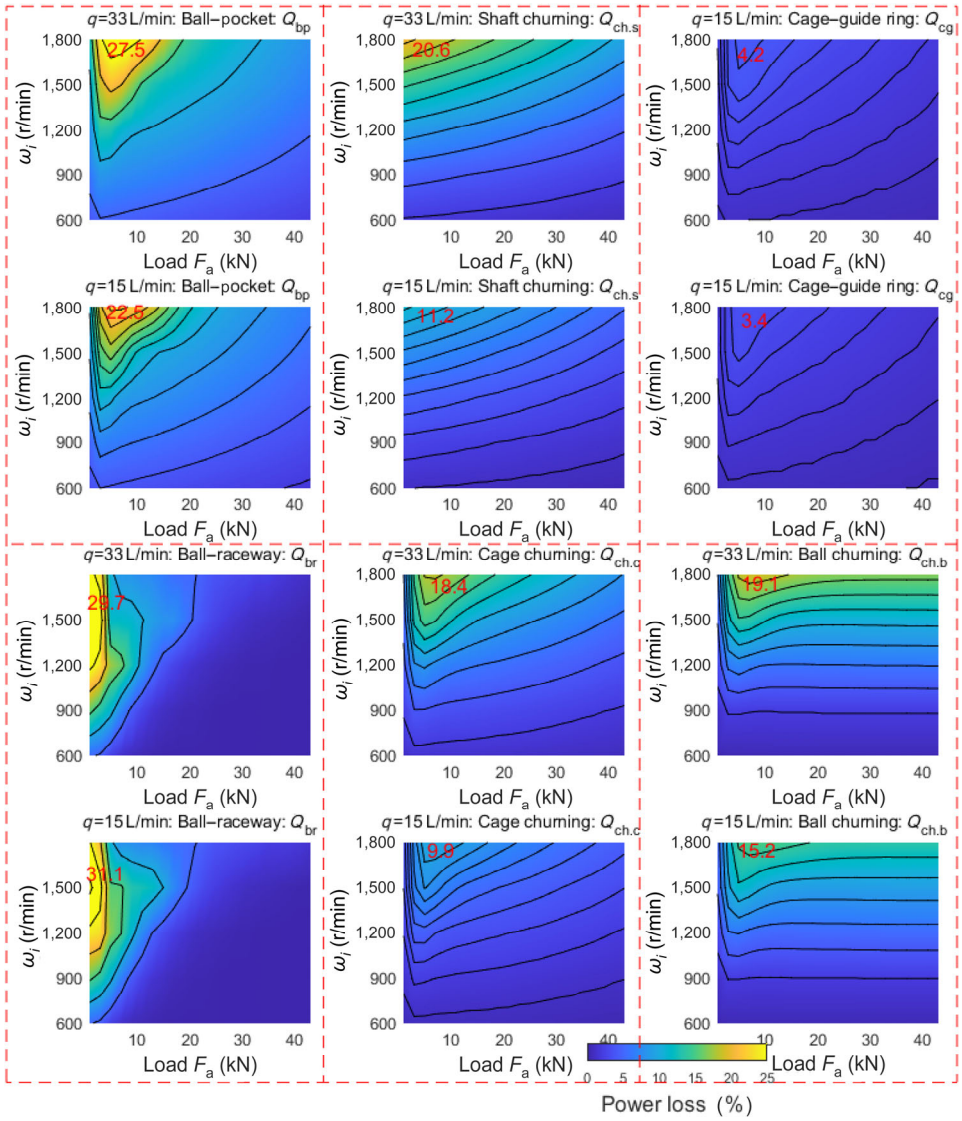

Fig. 17 Normalized power loss contour of six components; the red box shows the comparison of the results of the two oil flow rates.

tested bearings of the motor drive end and non-drive end under two oil flow rates q_{oil} =33 and 15 L/min are displayed. The initial temperature values used in the thermal network model were extracted from the test results at t=0 min. The temperature of the atmosphere was T_{atm} =35 °C. According to these ten groups of temperature test results, the simulation results show good agreement with the test, which indicates that the proposed heat generation model and thermal network model in this study are correct and reasonable.

The analysis of the temperature results can refer to the experimental loading procedures shown in Fig. 6. In general, as the running time increases, the bearing temperature tends to stabilize, especially at low speeds (ω_i =600 and 900 r/min). This can be explained by the following two reasons. First, in the later stage of each group of tests, as the axial load increases, the generated frictional heat gradually decreases and stabilizes, as shown in Fig. 16. Second, because the temperature difference between the bearing assembly and the external atmosphere ($T_h - T_{atm}$) increases at high temperatures, the heat dissipation rate is higher than that at low temperatures. Because the initial temperature of each group of tests is different, the initial temperature is marked with a dashed line in Fig. 18 to facilitate the comparison of temperature rises. It should be noted that in the medium- and high-speed (ω_i =1,500 and 1,800 r/min) tests, the

temperature rises rapidly at the beginning of the test, as marked by the black ellipse in Fig. 18. This is because the degree of skidding and over-skidding is significantly high at this stage. The frictional power loss shown in Fig. 16 is also the most prominent at this stage.

Using the experimental results in Fig. 18, Fig. 19 analyzes the maximum temperature and temperature rise for each rotational speed test. It can be seen that at the flow rate of oil q_{oil} = 33 L/min, the maximum temperature and the temperature rise are generally lower than that at q_{oil} =15 L/min. Because the initial temperature of the test is different, it is more reasonable to analyze the temperature rise value. The temperature rise shows an approximately linear increasing trend with an increase in speed. The temperatures of the bearings at the drive end and the non-drive end are generally close.

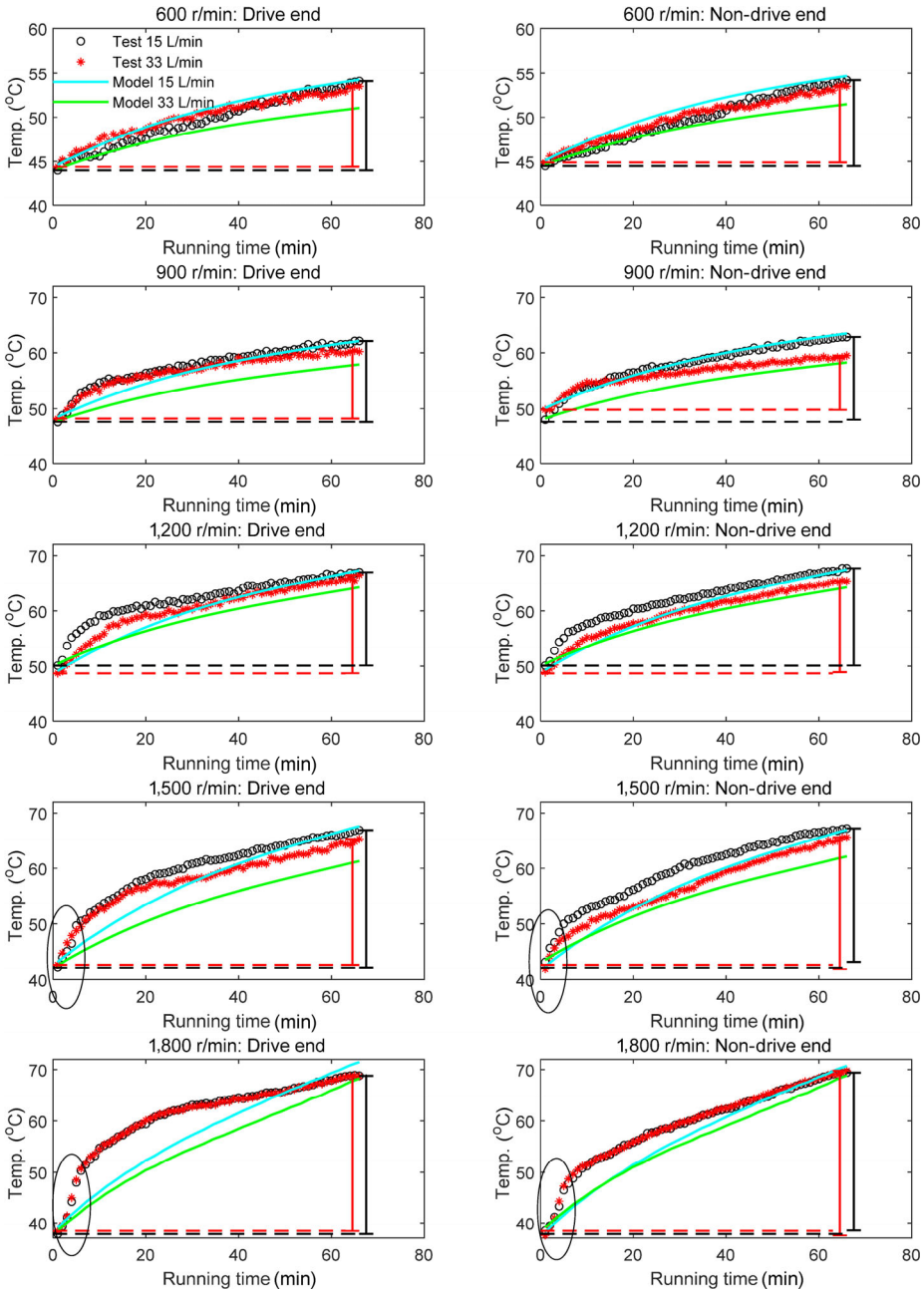

Fig. 18 Comparison of tested and calculated temperature values by the thermal network method. The test points on the motor drive end and non-drive end are displayed, respectively.

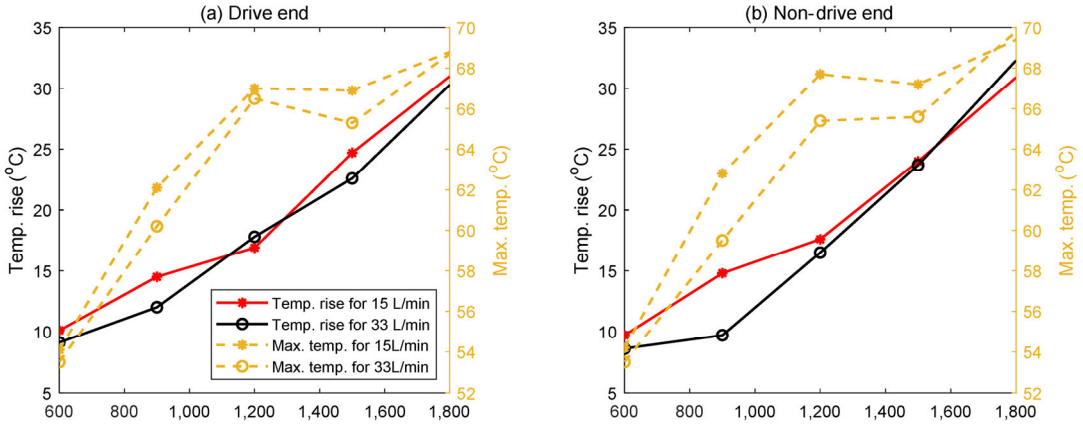

Fig. 19 Maximum temperature and temperature rise after running the test bearing for 66 min.

5 Conclusions

Ten groups of tests of an FPCB with a bore diameter of 220 mm were conducted in this work. The effects of rotational speed, axial load, and oil injection flow rate on the occurrence of over-skidding were theoretically and experimentally discussed. The integrated heat generation model and the thermal network model were validated by the test results, and the heat generation by different bearing components and the temperature rise were subsequently calculated. The relationship between over-skidding and vibration features was first proposed by the author. The following conclusions were drawn:

1) The maximum degree of over-skidding decreases with a decrease in rotational speed, and the required axial load for the ball changing from over-skidding to pure rolling is reduced.

2) The degrees of over-skidding and skidding are well reflected by the featured frequency of the envelope spectra of the vibration signal, providing a way to indirectly measure the degree of over-skidding.

3) The variation in the total power loss is consistent with the trend in the value of CSR as the axial load increases. The friction power loss of the ball–pocket is close to 30%, which is significant in the working conditions of over-skidding.

Acknowledgements

This research was supported in part by a scholarship from the China Scholarship Council (CSC) (No. 201806880007), the National Natural Science Foundation of China (No. 11872222), and the State Key Laboratory of Tribology (No. SKLT2021D11). The Italian Ministry of Education, University and Research is acknowledged for the support provided by the Project "Department of Excellence LIS4.0 - Lightweight and Smart Structures for Industry 4.0".

References

[1] Harris T A, Kotzalas M N. *Advanced Concepts of Bearing Technology: Rolling Bearing Analysis*. Boca Raton: CRC Press, 2006.

[2] Cao H R, Wang D, Zhu Y B, Chen X F. Dynamic modeling and abnormal contact analysis of rolling ball bearings with

double half-inner rings. *Mech Syst Signal Process* **147**: 107075 (2021)

[3] Gao S, Chatterton S, Naldi L, Pennacchi P. Ball bearing skidding and over-skidding in large-scale angular contact ball bearings: Nonlinear dynamic model with thermal effects and experimental results. *Mech Syst Signal Process* **147**: 107120 (2021)

[4] Han Q K, Chu F L. Nonlinear dynamic model for skidding behavior of angular contact ball bearings. *J Sound Vib* **354**: 219–235 (2015)

[5] Gao S, Chatterton S, Pennacchi P, Han Q K, Chu F L. Skidding and cage whirling of angular contact ball bearings: Kinematic-hertzian contact-thermal-elasto-hydrodynamic model with thermal expansion and experimental validation. *Mech Syst Signal Process* **166**: 108427 (2022)

[6] Tu W B, Yu W N, Shao Y M, Yu Y Q. A nonlinear dynamic vibration model of cylindrical roller bearing considering skidding. *Nonlinear Dyn* **103**(3): 2299–2313 (2021)

[7] Yan C, Lin J, Liang K X, Ma Z P, Zhang Z Q. Tacholess skidding evaluation and fault feature enhancement base on a two-step speed estimation method for rolling bearings. *Mech Syst Signal Process* **162**: 108017 (2022)

[8] Yan C, Zhao M, Lin J, Liang K X, Zhiqiang Zhang. Fault signature enhancement and skidding evaluation of rolling bearing based on estimating the phase of the impulse envelope signal. *J Sound Vib* **485**: 115529 (2020)

[9] Gao S, Han Q K, Zhou N N, Pennacchi P, Chu F L. Stability and skidding behavior of spacecraft porous oil-containing polyimide cages based on high-speed photography technology. *Tribol Int* **165**: 107294 (2022)

[10] Fang B, Zhang J H, Wan S K, Hong J. Determination of optimum preload considering the skidding and thermal characteristic of high-speed angular contact ball bearing. *J Mech Des* **140**(5): 053301 (2018)

[11] Xu C, Li B, Wu T H. Wear characterization under sliding–rolling contact using friction-induced vibration features. *Proc Inst Mech Eng Part J J Eng Tribol* **236**(4): 634–647 (2022)

[12] Li J N, Chen W, Xie Y B. Experimental study on skid damage of cylindrical roller bearing considering thermal effect. *Proc Inst Mech Eng Part J J Eng Tribol* **228**(10): 1036–1046 (2014)

[13] Vidyasagar K E C, Pandey R K, Kalyanasundaram D. An exploration of frictional and vibrational behaviors of textured deep groove ball bearing in the vicinity of requisite minimum load. *Friction* **9**(6): 1749–1765 (2021)

[14] Li J N, Xue J F, Ma Z T. Study on the thermal distribution characteristics of high-speed and light-load rolling bearing considering skidding. *Appl Sci* **8**(9): 1593 (2018)

[15] Liu Y Q, Chen Z G, Tang L, Zhai W M. Skidding dynamic performance of rolling bearing with cage flexibility under accelerating conditions. *Mech Syst Signal Process* **150**: 107257 (2021)

[16] Pasdari M, Gentle C R. Effect of lubricant starvation on the minimum load condition in a thrust-loaded ball bearing. *Tribol Trans* **30**(3): 355–359 (1987)

[17] Wen B. Theoretical and experimental investigation of cage dynamics in angular contact ball bearing. Ph.D. Thesis. Dalian (China): Dalian University of Technology, 2017.

[18] Gao S, Han Q K, Zhou N N, Pennacchi P, Chatterton S, Qing T, Zhang J Y, Chu F L. Experimental and theoretical approaches for determining cage motion dynamic characteristics of angular contact ball bearings considering whirling and overall skidding behaviors. *Mech Syst Signal Process* **168**: 108704 (2022)

[19] Xie Z J, Wang Y, Wu R S, Yin J H, Yu D, Liu J Q, Cheng T H. A high-speed and long-life triboelectric sensor with charge supplement for monitoring the speed and skidding of rolling bearing. *Nano Energy* **92**: 106747 (2022)

[20] Han Q K, Ding Z, Qin Z Y, Wang T Y, Xu X P, Chu F L. A triboelectric rolling ball bearing with self-powering and self-sensing capabilities. *Nano Energy* **67**: 104277 (2020)

[21] Liu Y, Zhang Z. Skidding research of a high-speed cylindrical roller bearing with beveled cage pockets. *Ind Lubr Tribol* **72**(7): 969–976 (2020)

[22] Niu L K, Cao H R, He Z J, Li Y M. An investigation on the occurrence of stable cage whirl motions in ball bearings based on dynamic simulations. *Tribol Int* **103**: 12–24 (2016)

[23] Gupta P K. Dynamics of rolling-element bearings part III: Ball bearing analysis. *J Lubr Tech* **101**(3): 312–318 (1979)

[24] Gupta P K. Dynamics of rolling-element bearings—Part IV: Ball bearing results. *J Lubr Tech* **101**(3): 319–326 (1979)

[25] Kingsbury E P. Torque variations in instrument ball bearings. *Tribol Trans* **8**(4): 435–441 (1965)

[26] Ma F B, Li Z M, Qiu S C, Wu B J, An Q. Transient thermal analysis of grease-lubricated spherical roller bearings. *Tribol Int* **93**: 115–123 (2016)

[27] Yan K, Hong J, Zhang J H, Mi W, Wu W W. Thermal-deformation coupling in thermal network for transient analysis of spindle-bearing system. *Int J Therm Sci* **104**: 1–12 (2016)

[28] Wang Y, Cao J C, Tong Q B, An G P, Liu R F, Zhang Y H, Yan H. Study on the thermal performance and temperature distribution of ball bearings in the traction motor of a high-speed EMU. *Appl Sci* **10**(12): 4373 (2020)

[29] Ai S Y, Wang W Z, Wang Y L, Zhao Z Q. Temperature rise of double-row tapered roller bearings analyzed with the thermal network method. *Tribol Int* **87**: 11–22 (2015)

[30] Zheng D X, Chen W F. Thermal performances on angular

contact ball bearing of high-speed spindle considering structural constraints under oil-air lubrication. *Tribol Int* **109**: 593–601 (2017)

[31] Pouly F, Changenet C, Ville F, Velex P, Damiens B. Power loss predictions in high-speed rolling element bearings using thermal networks. *Tribol Trans* **53**(6): 957–967 (2010)

[32] Takabi J, Khonsari M M. Experimental testing and thermal analysis of ball bearings. *Tribiol Int* **60**: 93–103 (2014)

[33] Li H, Li H, Liu Y, Liu H. Dynamic characteristics of ball bearing with flexible cage lintel and wear. *Eng Fail Anal* **117**: 104956 (2020)

[34] Walters C T. The dynamics of ball bearings. *J Lubr Technol* **93**(1): 1–10 (1971)

[35] Sander D E, Allmaier H, Priebsch H H, Reich F M, Witt M, Füllenbach T, Skiadas A, Brouwer L, Schwarze H. Impact of high pressure and shear thinning on journal bearing friction. *Tribol Int* **81**: 29–37 (2015)

[36] Jain S. Skidding and fault detection in the bearings of wind-turbine gearboxes. Ph.D. Thesis. Cambridge (United Kingdom): Cambridge University, 2012.

[37] Harris T A. An analytical method to predict skidding in high speed roller bearings. *S L E Trans* **9**(3): 229–241 (1966)

[38] Rumbarger J H, Filetti E G, Gubernick D. Gas turbine engine mainshaft roller bearing-system analysis. *J Lubr Technol* **95**(4): 401–416 (1973)

[39] Wang Y L, Wang W Z, Zhang S G, Zhao Z Q. Investigation of skidding in angular contact ball bearings under high speed. *Tribol Int* **92**: 404–417 (2015)

[40] Moazen Ahmadi A, Howard C Q, Petersen D. The path of rolling elements in defective bearings: Observations, analysis and methods to estimate spall size. *J Sound Vib* **366**: 277–292 (2016)

[41] Gao S, Chatterton S, Pennacchi P, Chu F L. Behaviour of an angular contact ball bearing with three-dimensional cubic-like defect: A comprehensive non-linear dynamic model for predicting vibration response. *Mech Mach Theory* **163**: 104376 (2021)

[42] Jiang Y C, Huang W T, Luo J N, Wang W J. An improved dynamic model of defective bearings considering the three-dimensional geometric relationship between the rolling element and defect area. *Mech Syst Signal Process* **129**: 694–716 (2019)

Shuai GAO. He received the B.S. and M.S. degrees in mechanical engineering from Beijing University of Chemical Engineering, Beijing, China, in 2015 and 2018, respectively. He was a visiting scholar in the Department of Mechanical Engineering at Tsinghua University, Beijing, China. He is currently a Ph.D. candidate in Department of Mechanical Engineering at Politecnico di Milano, Italy. His research interests focus on dynamics and fault diagnosis of rolling bearings.

Qinkai HAN. He is currently an associate professor in Department of Mechanical Engineering at Tsinghua University. He received his bachelor degree in aircraft engineering (2004) and Ph.D. degree from College of Energy and Power Engineering (2010) at Beihang University. During 2017–2018, he was a postdoctoral research fellow at Purdue University, West Lafayette, IN, USA. His interests focus on dynamics and fault diagnosis of rolling bearings and development of self-powered system based on triboelectric nanogenerator.